J. Fluid Mech. (2020), *vol.* 895, A1. © The Author(s), 2020.
Published by Cambridge University Press
doi:10.1017/jfm.2020.281

Streaming controlled by meniscus shape

Y. Huang[1,2,†], C. L. P. Wolfe[2], J. Zhang[3,4] and J.-Q. Zhong[1,†]

[1]School of Physics Science and Engineering, Tongji University, Shanghai 200092, China

[2]School of Marine and Atmospheric Sciences, Stony Brook University, Stony Brook 11794, USA

[3]NYU-ECNU Institute of Physics, New York University Shanghai, Shanghai 200062, China

[4]Department of Physics & Courant Institute, New York University, New York 10012, USA

(Received 14 August 2019; revised 19 March 2020; accepted 5 April 2020)

Surface waves called meniscus waves often appear in systems that are close to the capillary length scale. Since the meniscus shape determines the form of the meniscus waves, the resulting streaming circulation has features distinct from those caused by other capillary–gravity waves recently reported in the literature. In the present study, we produce symmetric and antisymmetric meniscus shapes by controlling boundary wettability and excite meniscus waves by oscillating the meniscus vertically. The symmetric and antisymmetric configurations produce different surface capillary–gravity wave modes and streaming flow structures. The root-mean-square speed of the streaming circulation increases with the second power of the forcing amplitude in both configurations. The flow symmetry of streaming circulation is retained under the symmetric meniscus, while it is lost under the antisymmetric meniscus. The streaming circulation pattern beneath the meniscus observed in our experiments is qualitatively explained using the method introduced by Nicolás & Vega (*Fluid Dyn. Res.*, vol. 32 (4), 2003, pp. 119–139) and Gordillo & Mujica (*J. Fluid Mech.*, vol. 754, 2014, pp. 590–604).

Key words: surface gravity waves, capillary waves

1. Introduction

Steady streaming is a wave-induced residual flow driven by Reynolds stresses and balanced by viscous stresses in the Stokes boundary layer (Batchelor 2000; Riley 2001). The momentum of the streaming flow in the boundary layer can be transferred into the liquid bulk through fluid viscosity to form an Eulerian mean circulation. Streaming circulations play essential roles in fluid mass and passive scalar transport in many environments, such as inside blood vessels, cochleae and the boundary layer over ocean sediments (Lesser & Berkley 1972; Schneck & Walburn 1976; Holmedal & Myrhaug 2009). In recent years, the residual motion driven by surface waves has also been used to control the distribution of suspended particles (Chen *et al.* 2014; Punzmann *et al.* 2014; Francois *et al.* 2017). A more complete understanding of the underlying physical mechanisms that control the formation of streaming circulations is likely to be beneficial to these applications.

† Email addresses for correspondence: yicheng.huang@stonybrook.edu, jinqiang@tongji.edu.cn

https://doi.org/10.1017/jfm.2020.281 Published online by Cambridge University Press

In this paper, we investigate the streaming flows inside a fluid system with an overlying free surface and a horizontal scale one order of magnitude larger than the capillary length, l_c. When such a system is oscillated vertically, a variety of standing surface waves can be generated by the capillary effect (Lucassen-Reynders & Lucassen 1970; Perlin & Schultz 2000). The most well-known type of waves are Faraday waves (Faraday 1831; Miles & Henderson 1990), which are excited by parametric instability. However, even when the system is stable to Faraday waves, one transverse surface wave is still observed if there is a static meniscus. This meniscus wave (Strickland, Shearer & Daniels 2015) is driven by periodic perturbations to hydrostatic balance due to the vertical oscillations. The resultant surface pressure anomaly deforms the liquid–air interface periodically, forcing a capillary–gravity wave (Douady 1990). Up to now, there has been a lack of experiments that directly observe meniscus waves and their induced streaming circulation, since meniscus waves are usually entangled with Faraday waves in most previous experiments (Douady 1990; Strickland *et al.* 2015).

Streaming flows can occur along the free surface due to the nonlinearity of surface deformations and the velocity field (Longuet-Higgins 1953; Nicolás & Vega 2003). In these systems, the geometry of the meniscus increases the complexity of the streaming flow. Surfactants can promote the generation of streaming flows along the free surface by enhancing surface dissipation and tangential stress (Martín & Vega 2006). In the fully contaminated limit, the streaming boundary layer generated by the free surface behaves in the same manner as that caused by an elastic solid surface (Périnet *et al.* 2017; Moisy, Bouvard & Herreman 2018). How the static meniscus shape affects the streaming circulation structure in this limit remains an open question of great interest.

In the following sections, we present measurements of meniscus waves and the resultant streaming circulation under an oscillatory free surface. These measurements are performed in a fluid system where the Faraday waves are inhibited. By selecting the wettability of the lateral boundaries, we develop two kinds of meniscus with distinct symmetries. When the lateral walls are both hydrophilic, a symmetric meniscus with two identical acute angles is created. The resultant two-node linear meniscus wave gives rise to a four-eddy streaming circulation pattern. Alternatively, the meniscus has an antisymmetric shape in a hydrophilic–hydrophobic wetting configuration. In this case, the resultant linear meniscus wave has a single node and a double-eddy streaming circulation pattern is produced. The root-mean-square (r.m.s.) speed of the streaming circulation scales like $v_{rms} \sim (a_0/g_0)^2$, where a_0 is the forcing acceleration and g_0 is the gravitational acceleration. The single power function indicates a single dynamical regime over the parameter range studied. Remarkably, we further discover that, for the two meniscus shapes we use, the left–right symmetry of the streaming flow pattern differs markedly under various forcing amplitudes a_0/g_0. For the symmetric case, the streaming pattern remains highly symmetric in the full range of the applied forcing amplitude. In the antisymmetric case, however, the streaming pattern becomes less symmetric as a_0/g_0 increases owing to the interaction between the static meniscus profile and the meniscus wave. To explain these observations, we establish a simple analytical model to estimate the meniscus wave at linear order. We then compute the streaming velocity distribution in the boundary layer following the method of Nicolás & Vega (2003) and Gordillo & Mujica (2014) and use this to drive a steady laminar flow model that reproduces the observed streaming velocity fields.

https://doi.org/10.1017/jfm.2020.281 Published online by Cambridge University Press

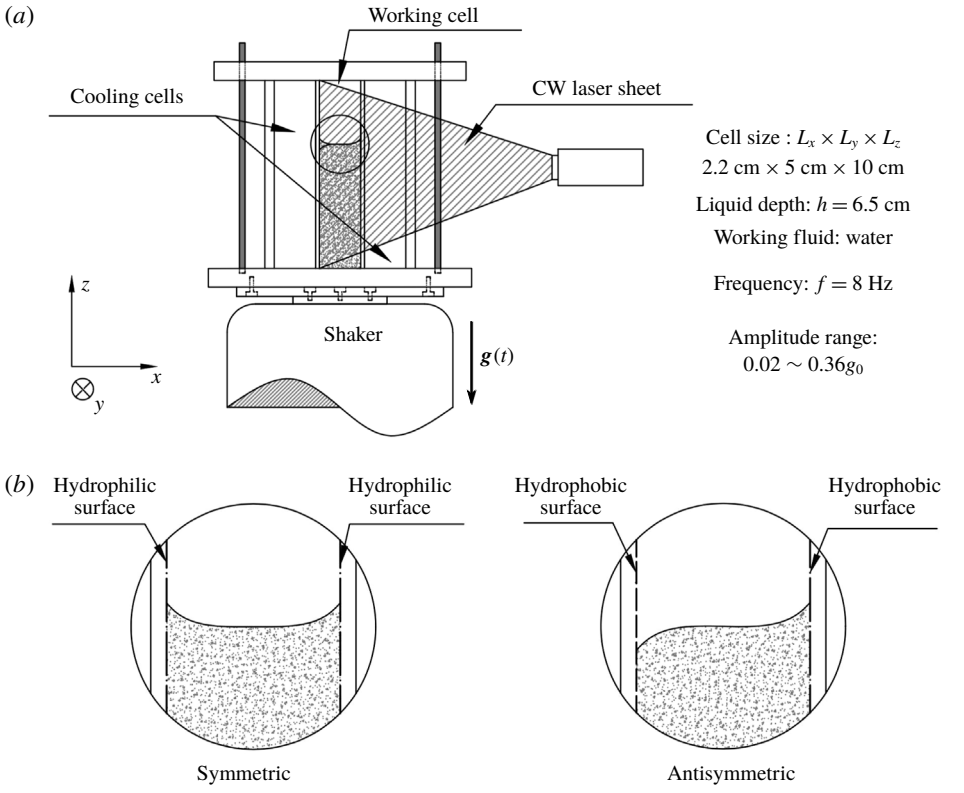


FIGURE 1. (*a*) Schematic drawing of the experimental apparatus. A water tank was oscillated sinusoidally in the z direction with a time-varying gravitational acceleration $g(t) = -(g_0 + a_0 \sin 2\pi f_0 t)$. The tank was divided into three cells by two SiO_2 glass plates. The fluid velocity field was measured in the working cell using PIV. A DPSS laser sheet illuminated the seeding particles in the working cell at $y = 2.5$ cm and the particle motion was recorded by a high-speed camera. (*b*) Schematic of meniscus in symmetric and antisymmetric configurations.

2. Experiment

2.1. *Experimental set-up*

In the experiment, we used a rectangular Plexiglas tank divided into three cells by two optical glass plates (figure 1*a*). The middle cell was the working cell, with the dimensions $L_x = 2.2$ cm in length, $L_y = 5.0$ cm in width and $L_z = 10.0$ cm in height. Deionized water filled the working cell to a depth of $h = 6.5$ cm. Two types of meniscus symmetry were created by selecting the wettability conditions of the glass plates (see figure 1*b*). The clean optical glass surface was hydrophilic, with a contact angle close to 45°. A hydrophobic boundary was made by applying a coating of hydrophobic nano-SiO_2 film (CHEMNANO®, NC317) to an optical glass surface, creating a contact angle close to 135°. A working cell with two hydrophilic lateral boundaries creates the symmetric setting, while choosing one boundary hydrophobic and the other hydrophilic creates an antisymmetric system. We chose experiments that had contact angles closest to the ideally symmetric and antisymmetric cases. In the chosen symmetric case, the left contact angle is $\theta_l = 44.01°$ (43.71°, 48.02°) and the

https://doi.org/10.1017/jfm.2020.281 Published online by Cambridge University Press

right contact angle is $\theta_r = 48.57°$ (46.18°, 50.75°). In the chosen antisymmetric case, the left contact angle is $\theta_l = 142.66°$ (137.41°, 146.92°) and the right contact angle is $\theta_r = 45.84°$ (43.65°, 47.86°). The numbers in parentheses are the 95 % confidence intervals. The contact angle of water with the remaining Plexiglas boundary was close to 90°.

The fluid tank was installed on an electrodynamic shaker (Labworks® ET-139) that vibrated sinusoidally in the z direction with an excess gravitational acceleration varying from $0.02g_0$ to $0.36g_0$ and a frequency of $f_0 = 8$ Hz. The control signal produced from a wavefunction generator was amplified using a linear power amplifier to drive the shaker. An accelerometer mounted on the base plate of the fluid tank (not shown in figure 1) measured the instantaneous acceleration, which was fed back to the wavefunction generator to regulate the control signal. The closed-loop control system reduced error and ensured the stability of the shaker oscillation.

We measured the fluid velocity field in the working cell using a particle imaging velocimetry (PIV) system. Neutrally buoyant hollow glass microspheres of diameter 10 μm (DANTEC®, HGS-10) were seeded in the flow. Because of the effect of surface tension, some of the seeding particles were suspended on the free surface. We used these particles to track the surface deformation (see § 2.2). We found that these surface particles also played a role in enhancing surface damping and surface-deformation-induced streaming. The PIV particles in the system were illuminated from the right using a continuous, diode-pumped solid-state (DPSS) laser, creating a 1 mm thick light sheet that passed through the $y = 2.5$ cm plane. PIV images that cover a region from the surface to a fluid depth of approximately 3 cm were captured by a high-speed camera (Photron UX100) placed perpendicular to the laser sheet, at a frame rate of 80 Hz, achieving a time resolution of 10 frames per oscillation period. The surface oscillation caused by the primary flow is estimated by measuring the surface profile deformation in one period. Two-dimensional velocity maps for the secondary flow were obtained by cross-correlating two images with the same phase in two consecutive periods using LaVision® PIV software. Each velocity vector was calculated from interrogation windows spanning 32 pixel × 32 pixel, with 50 % overlap of neighbouring sub-windows. Each vector covers a region of 16 pixel × 16 pixel and there are 80 × 64 velocity vectors per frame, achieving a spatial resolution of 0.34 mm (one order in magnitude smaller than the capillary length scale).

The laser light sheet may heat up the fluid on the right side of the working cell and give rise to an overturning circulation. The speed of this overturning flow could be up to the order of $O(10^{-3}$ cm s$^{-1})$, comparable to the speed of the streaming flow we study. To avoid this laser-induced convection, the two lateral cells were filled with water to reduce the thermal heating of the fluid in the working cell. With this thermal protection, the speed of the overturning flow was reduced to $O(10^{-5}$ cm s$^{-1})$ and was negligible.

2.2. *Observation of the surface deformation*

The time-varying acceleration of the fluid tank in the laboratory frame is $a(t) = a_0 \sin\varphi(t)$, where a_0 is the forcing amplitude and $\varphi(t) = 2\pi f_0 t$ is the oscillation phase. From Newton's third law, the effective gravity felt by the fluid in the tank is

$$g(t) = -[g_0 + a_0 \sin\varphi(t)],$$

in which g_0 is the gravitational acceleration constant. When $\varphi = \pi/2$, the fluid tank is at its highest position with maximum super-gravity; when $\varphi = 3\pi/2$, the tank is at its

https://doi.org/10.1017/jfm.2020.281 Published online by Cambridge University Press

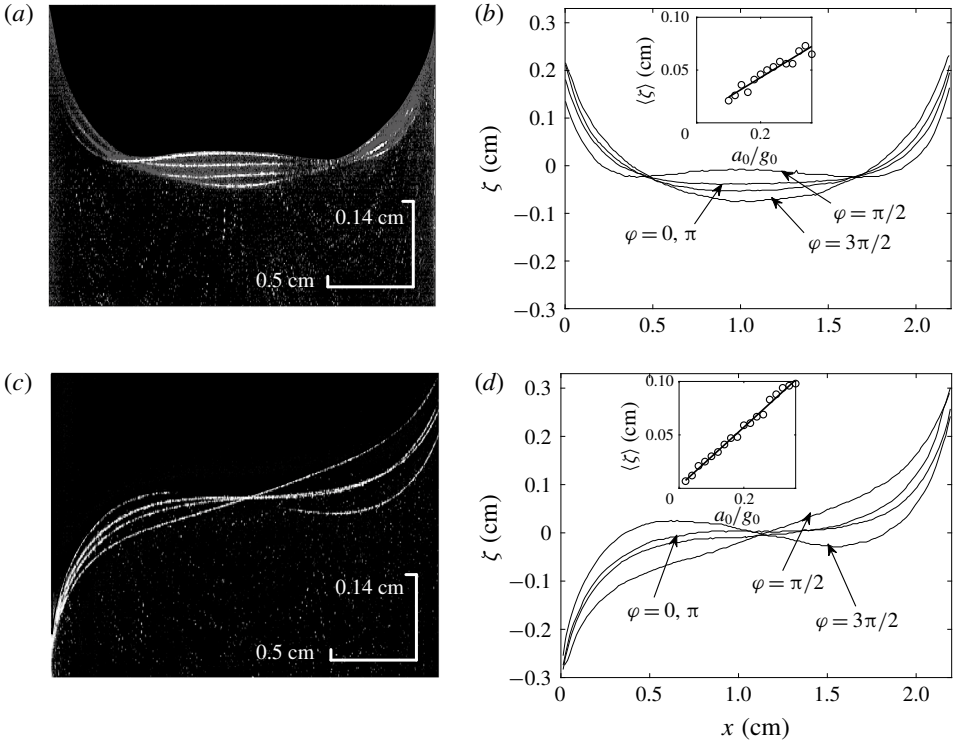


FIGURE 2. Images and surface profiles of meniscus shape deformation at $\varphi = 0$, $\pi/2$, π and $3\pi/2$, with $f_0 = 8$ Hz and $a_0 = 0.2g_0$. (*a*) A PIV image of the vibrating surface in the symmetric configuration. (*b*) The extracted surface profiles corresponding to (*a*). (*c*) A PIV image of the vibrating surface in the antisymmetric configuration. (*d*) The extracted surface profiles of symmetric scenario corresponding to (*c*). The insets in (*b*) and (*d*) show the horizontally averaged surface deformation amplitude $\langle\zeta\rangle$ as a function of a_0/g_0. The symbols in the insets are experimental measurements and the solid line is a linear regression.

lowest position with maximum sub-gravity. To force the system without exciting the Faraday instability, we select $f_0 = 8.0$ Hz and $0.02 \leqslant a_0/g_0 \leqslant 0.36$ (see appendix B). Thus the periodic deformation of the liquid–air interface excites the cavity modes, giving rise to standing meniscus waves. We observe that such a surface deformation mode is strongly dependent on the geometry of the static meniscus. To quantify the relation between this surface deformation mode and the shape of the static meniscus, we measure the surface profile in different oscillation phases from the PIV images. It is found that a large proportion of the liquid–air interface is clearly visible due to seeding particles accumulated at the interface, which are illuminated by the laser sheet (figure 2*a*,*c*). The free surface is tracked using light intensity: particles are densely populated on the free surface so the light intensity is maximal there. Using this method, we extract the surface profiles $\zeta(x)$ at four oscillatory phases, $\varphi = 0$, $\pi/2$, π and $3\pi/2$, as shown in figure 2(*b*) and 2(*d*).

The meniscus oscillates at the forcing frequency f_0. The response of meniscus wave amplitude $\zeta(x)$ to the forcing acceleration amplitude a_0/g_0 is estimated by the

https://doi.org/10.1017/jfm.2020.281 Published online by Cambridge University Press

horizontally averaged surface deformation amplitude $\langle\zeta\rangle$, which is defined by

$$\langle\zeta\rangle = \overline{|\zeta_{\varphi=\pi/2} - \zeta_{\varphi=3\pi/2}|},$$

where $\zeta_{\varphi=\pi/2}$ and $\zeta_{\varphi=3\pi/2}$ are the surface profiles captured at $\varphi = \pi/2$ and $\varphi = 3\pi/2$, respectively; the overline denotes an average in the x direction. The mean amplitude of the meniscus oscillation $\langle\zeta\rangle$ grows linearly with the forcing amplitude (see the insets figure 2*b*,*d*). The scale for the speed of the primary flow is $\omega\langle\zeta\rangle$, which ranges from 0.5 cm s^{-1} to 5 cm s^{-1}. The Reynolds number for the primary flow, $Re = \omega\langle\zeta\rangle L/\nu$, therefore ranges from 110 to 1100, and we can infer that the effect of viscosity on the primary oscillation is weak. In the symmetric case, the excited mode is symmetric and has two nodes. At maximum super-gravity ($\varphi = \pi/2$) the liquid surface bulges upwards in the middle of the cell, analogous to the phenomenon of the liquid jet observed by Antkowiak *et al.* (2007). At maximum sub-gravity ($\varphi = 3\pi/2$), the meniscus bends downwards to its greatest extent. Between these two states, the fluid flows periodically between the lateral boundary and the middle of the cell. In the antisymmetric case, an oscillatory mode with one node at the centre ($x = L/2$) is instead excited. When the system is at maximum sub-gravity ($\varphi = 3\pi/2$), the fluid surface forms an 'S' shape, with the convex part on the hydrophobic side ($x < L/2$) and the concave part on the hydrophilic side ($x > L/2$). When the system is at maximum super-gravity ($\varphi = \pi/2$), the fluid surface approaches a straight slope. Between these two states, the fluid sloshes between the two lateral boundaries. No observable surface oscillation is found in the y direction. Representing the mode number as (k, l), where k and l are positive integers denoting the mode number on x and y axes, respectively, the symmetric and antisymmetric configurations give rise to mode $(2, 0)$ and $(1, 0)$ waves, respectively.

2.3. *Observation of the streaming motion*

The streaming circulation is observed when the PIV images are broadcast stroboscopically. The streaming circulation is one order of magnitude weaker than the instantaneous primary flow. Once the circulation forms, it persists as long as the forcing oscillation continues. During the experiment, we collected the PIV images one minute after the forcing was turned on, when a steady streaming circulation had been established. The flow velocity and the vertical scale of the circulations, for both wettability configurations, appear to increase if the oscillation amplitude a_0 increases. The streaming circulation has distinct structures in symmetric and antisymmetric cases. The streaming circulation patterns are taken when $\varphi \approx \pi$, when the free surface is close to its equilibrium state.

In the symmetric case (figure 3), the secondary circulation has a stable four-vortex structure, with clockwise (anticlockwise) rotation near the right (left) lateral boundary. When $a_0 \sim 0.1g_0$, the central vortices are not clearly visible in the PIV image. As the forcing gets stronger, the central vortices become apparent with approximately circular streamlines. At the strongest forcing amplitude, the boundary vortices are well developed, whereas the central vortices become suppressed and asymmetric.

In the antisymmetric case, the secondary flow field has a dipole circulation structure with a weaker anticlockwise circulation near the hydrophobic side and a stronger clockwise circulation near the hydrophilic side (figure 4). When the forcing is weak, $a_0 \sim 0.1g_0$, the anticlockwise circulation is only partially visible in the PIV image, but a strong leftward velocity is found below the free surface. As the forcing amplitude

https://doi.org/10.1017/jfm.2020.281 Published online by Cambridge University Press

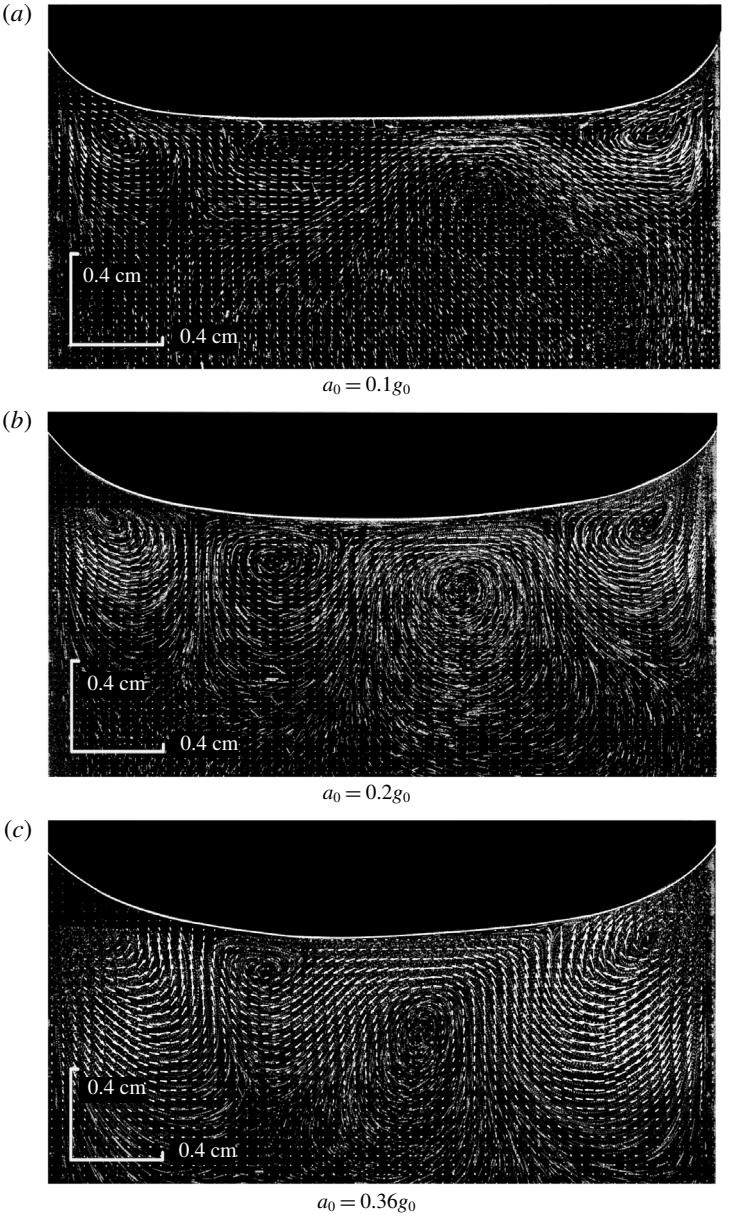


FIGURE 3. Velocity fields of the streaming flows overlying the raw PIV image in the symmetric case for three values of a_0. For each case, the driving frequency is $f_0 = 8$ Hz. The liquid–air interface has been highlighted manually. The streaming flows in (*a*), (*b*) and (*c*) are computed at the oscillation phases $\varphi = 9/10\pi$, $\varphi = 13/10\pi$ and $\varphi = 13/10\pi$, respectively.

https://doi.org/10.1017/jfm.2020.281 Published online by Cambridge University Press

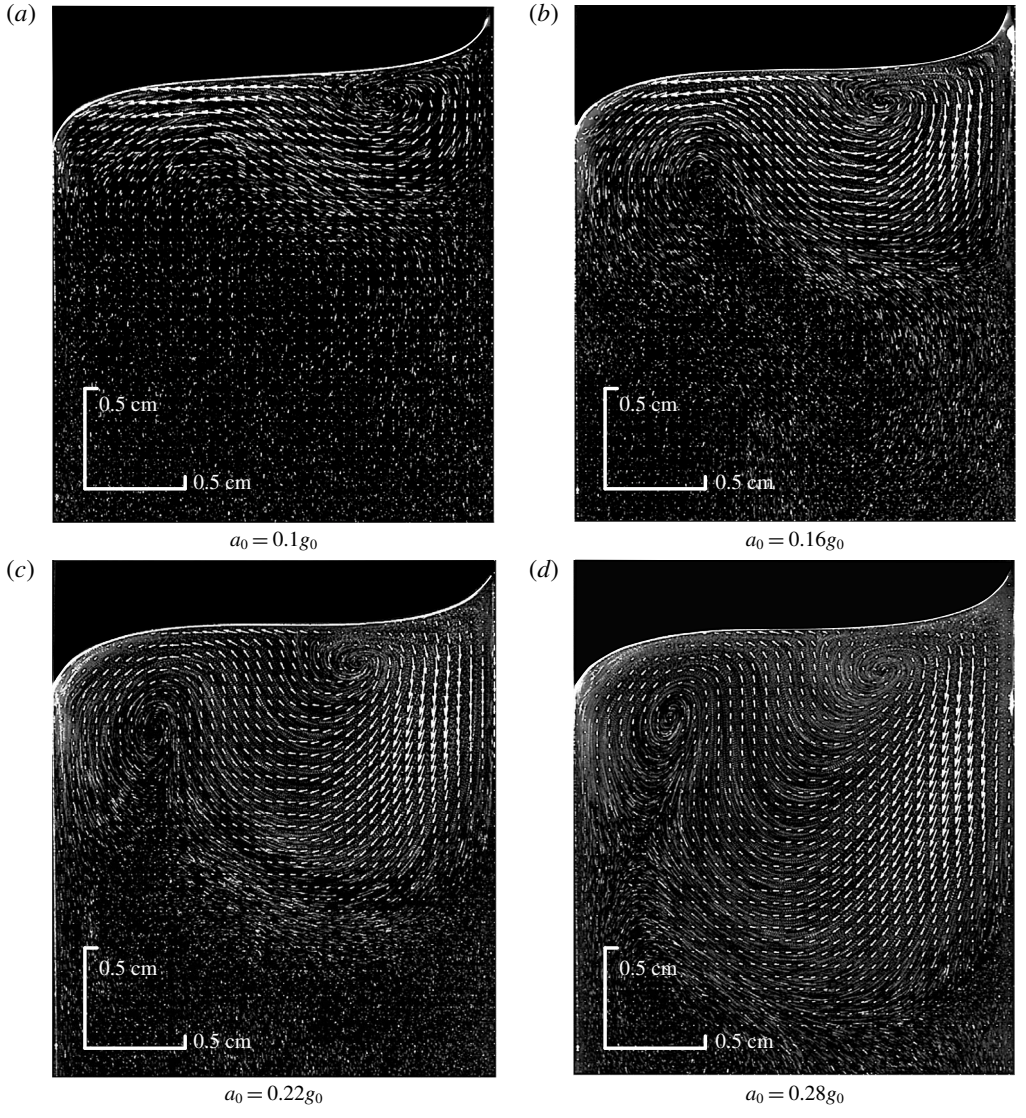


FIGURE 4. Velocity fields of the streaming flows overlying the raw PIV image in the antisymmetric case for four values of a_0. For each case, the driving frequency is $f_0 = 8$ Hz. The liquid–air interface has been highlighted manually. The streaming flows in (*a*), (*b*), (*c*) and (*d*) are computed at the oscillation phases $\varphi = 5/6\pi$, $\varphi = 9/10\pi$, $\varphi = 9/10\pi$ and $11/10\pi$, respectively.

increases, the anticlockwise circulation becomes more dominant and downward motion becomes more prominent near the hydrophobic side.

To quantify the dynamical behaviour of the secondary flow, we compute the r.m.s. fluid speed in the observed section:

$$v_{rms} = \frac{1}{A}\sqrt{\iint_A (u^2 + w^2)\,\mathrm{d}x\,\mathrm{d}z}. \tag{2.1}$$

https://doi.org/10.1017/jfm.2020.281 Published online by Cambridge University Press

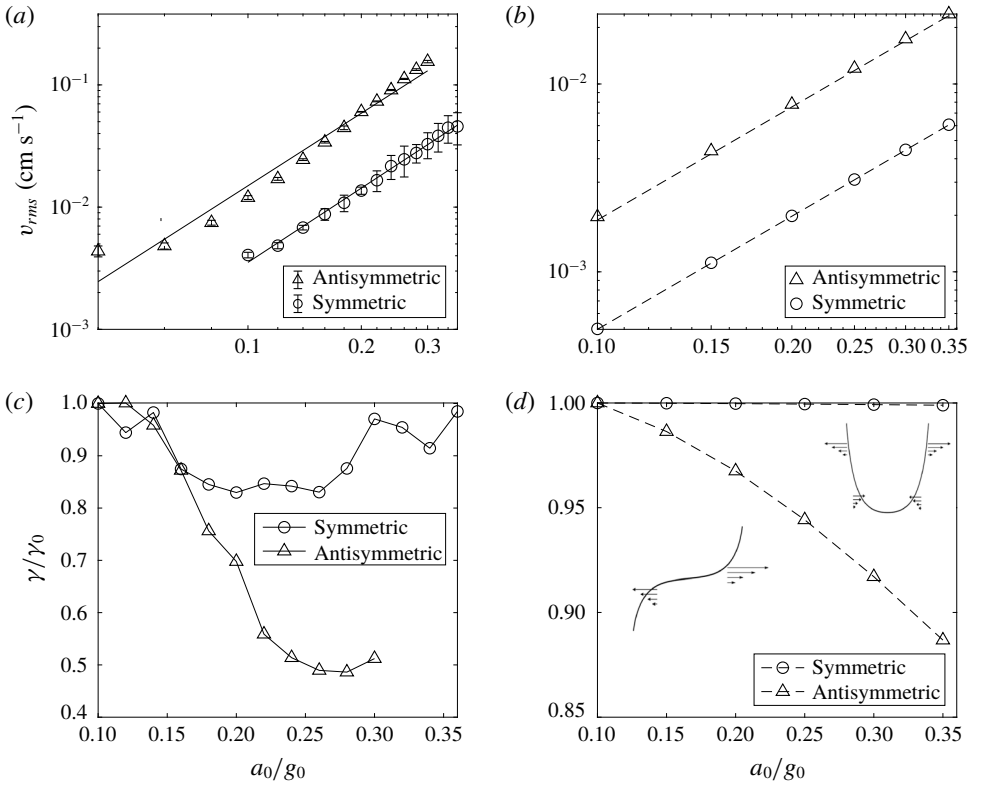


FIGURE 5. Response of the (*a*,*b*) r.m.s. speed, v_{rms}, and (*c*,*d*) symmetry parameter, γ/γ_0, to changes in forcing amplitude a_0/g_0 in (*a*,*c*) the laboratory experiments and (*b*,*d*) the simulations. The fitted trends in (*a*) have $\beta = 2.02$ and $\beta = 1.97$ for symmetric and antisymmetric cases, respectively, while the fitted trends in (*b*) both have $\beta = 2.0$. The symmetry parameter γ is defined in (2.3) and normalized by $\gamma_0 = \gamma|_{a_0/g_0=0.1}$. The insets in (*d*) show schematic plots illustrating the streaming velocity distribution under the free surface.

Here A is the total cross-sectional area of the observed fluid bulk, and u and w are the velocity components in the x and z directions, respectively. As shown in figure 5(*a*), the kinetic energy density for fully established secondary flow structure v_{rms} scales like

$$v_{rms} \sim (a_0/g_0)^{\beta}, \tag{2.2}$$

where $\beta \approx 2$ for both symmetric and antisymmetric cases. This indicates that the secondary circulation is caused by the quadratic nonlinearity of the velocity field, which is consistent with the direct numerical simulations of Carrión *et al.* (2017). Note that the flow velocity near the boundary is not resolvable by PIV, so the integration in (2.1) excludes the region within 0.034 cm of the lateral boundaries. Further, the camera does not capture the whole water bulk, so the integration covers the region $z > -1.79$ cm in the symmetric case and $z > -1.65$ cm in the antisymmetric case. To avoid edge effects from the bottom, we limit the maximum forcing amplitude so that the streaming velocity at the bottom edge of the observation window is never more than 10 % of the characteristic secondary flow speed in the bulk.

https://doi.org/10.1017/jfm.2020.281 Published online by Cambridge University Press

The spatial symmetry of the secondary circulation pattern is quantified by the symmetry parameter

$$\gamma = \frac{\displaystyle\iint_{x<L/2} \mathrm{d}x\,\mathrm{d}z\,|\Omega(x,z)|/A_{x<L/2}}{\displaystyle\iint_{x>L/2} \mathrm{d}x\,\mathrm{d}z\,|\Omega(x,z)|/A_{x>L/2}}, \tag{2.3}$$

which denotes the ratio of mean vorticity magnitude of the left region over that of the right region of the working cell. In (2.3), $|\Omega(x,z)|$ is the magnitude of the vorticity, and $A_{x>L/2}$ and $A_{x<L/2}$ are the liquid bulk areas at the right or left side, respectively, of $x = 1.1$ cm below the static meniscus. Figure 5(*b*,*d*) shows the variation of γ/γ_0 against a_0/g_0, where $\gamma_0 = \gamma|_{a_0/g_0=0.1}$ is a reference γ value. The variation of γ/γ_0 with forcing amplitude is different in the symmetric and antisymmetric cases. In the symmetric case, the secondary flows remains highly symmetric, with no obvious trend in γ/γ_0. In contrast, in the antisymmetric case, the symmetry parameter γ decreases rapidly as the forcing amplitude increases, then saturates at $\gamma \approx 0.5\gamma_0$ for large forcing amplitudes.

3. Theory

In this section, we develop a theoretical description of the meniscus wave and resulting secondary circulation. In order to simplify the analysis, we assume that the imaged flow is two-dimensional (2-D); that is, we neglect the effect of the front and back plates. We start by deriving the static shape of the meniscus and solve for the wave modes on this background state in § 3.1. The secondary circulation is obtained in § 3.2 by determining the streaming circulation along the free surface and lateral boundaries and using these as boundary conditions for a steady hydrodynamics solver.

3.1. *Meniscus wave*

The meniscus wave is solved by linearization of the ideal fluid equations with a free surface (e.g. Batchelor 2000). The nonlinear fluid equations are

$$\nabla^2\phi = 0, \tag{3.1}$$

$$\left[\partial_t\phi + \frac{1}{2}(\nabla\phi)^2\right]\Big|_{z=\zeta} + [g_0 + a_0\sin(\omega t)]\zeta = \frac{\sigma}{\rho}\frac{\partial^2_{xx}\zeta}{[1+(\partial_x\zeta)^2]^{3/2}}, \tag{3.2}$$

$$\partial_t\zeta + \partial_x\phi|_{z=\zeta}\partial_x\zeta = \partial_z\phi|_{z=\zeta}, \tag{3.3}$$

$$\phi|_{z\to-\infty} = 0, \tag{3.4}$$

$$\partial_x\phi|_{x=0,L} = 0, \tag{3.5}$$

where $\zeta = \zeta(x,t)$ is the surface elevation and $\phi = \phi(x,z,t)$ is the velocity potential field. The parameter notation is the same as in the previous section. The cell width is $L = 2.2$ cm, $g_0 = 980$ cm s^{-2} is the gravitational acceleration, $\rho = 1$ g cm^{-3} is the density of water, $\sigma = 72$ dyne cm^{-1} is the surface tension of water, a_0 is the forcing acceleration, and $\omega = 2\pi f_0$ is the forcing angular frequency.

The linearization is done in the following way. We use the capillary length $l_c = \sqrt{\sigma/(\rho g_0)} = 0.27$ cm as the characteristic length scale in the x and z directions. The scale of the surface displacement due to the forced oscillation is $a_0/\omega^2 \approx$

https://doi.org/10.1017/jfm.2020.281 Published online by Cambridge University Press

0.008–0.13 cm, so the ratio between these two length scales is a small dimensionless number, $\epsilon = a_0/(l_c\omega^2) \approx 0.03$–$0.5$, that scales the linear system response. In the experiment, the dimensionless forcing strength a_0/g_0 has the magnitude range of 0.02–0.36, which is $O(\epsilon)$. The mean static surface slope $\partial_x\zeta_0$ approaches zero at $x = 1.1$ cm and ≈ 1 at both boundaries. Nevertheless, to make progress, we assume that $\partial_x\zeta_0 \sim O(\epsilon)$ everywhere, while acknowledging that this will lead to errors near the boundaries. After scaling the velocity potential, ϕ, by g_0a_0/ω^3, the solution of the ideal fluid equations (3.1)–(3.5) can be expanded in an asymptotic series in powers of ϵ:

$$\zeta = \zeta_0 + \zeta_1, \tag{3.6}$$

$$\phi = \phi_0 + \phi_1. \tag{3.7}$$

The quantities with the subscript 0 are $O(1)$, which represents a situation when the forcing is neglected and depicts the static balance in the fluid bulk. Thus, both ϕ_0 and ζ_0 are independent of time. The quantities with subscript 1, that is, $O(\epsilon)$, represent the linear wave forced by the vertical oscillation. As the depth is three times larger than the cell width, we apply an infinite-depth bottom boundary condition.

3.1.1. *Zeroth-order solution*

At $O(1)$, equations (3.1) and (3.2) become the Young–Laplace equation:

$$\partial_{xx}^2\zeta_0 = \frac{\rho g_0}{\sigma}(\zeta_0 - z^*). \tag{3.8}$$

Since the left plate and right plate completely prevent liquid mass exchange, the experiment is done with total fluid volume conserved. The reference elevation,

$$z^* = -\frac{\sigma}{\rho g_0 L}(\partial_x\zeta_0|_{x=L} - \partial_x\zeta_0|_{x=0}) = -\frac{\sigma}{\rho g_0 L}[\tan(\theta_r) - \tan(\pi/2 - \theta_l)], \tag{3.9}$$

is determined by integrating equation (3.8) in x, applying the lateral boundary conditions, and requiring that the horizontal integral of ζ_0 vanish. The quantities θ_l and θ_r are the contact angles at the left and right boundaries, respectively. Following the experimental set-up, in the symmetric case $\theta_l = \theta_r = 45°$, and in the antisymmetric case $\theta_l = 135°$ and $\theta_r = 45°$. The corresponding boundary conditions for (3.8) are written as

$$\partial_x\zeta_0|_{x=0} = -s, \tag{3.10}$$

$$\partial_x\zeta_0|_{x=L} = 1. \tag{3.11}$$

Here, s controls the symmetry of the meniscus; it is 1 in the symmetric case and -1 in the antisymmetric case. These boundary conditions and the above zeroth-order equation are satisfied by

$$\zeta_0 = \frac{1 + s\cosh(mL)}{m\sinh(mL)}\cosh(mx) - \frac{s}{m}\sinh(mx) + z^*, \tag{3.12}$$

where $m = l_c^{-1}$. In figure 7, the solutions are compared to the static surface profile measurements for both symmetric and antisymmetric cases – the theoretical result captures the shape of the free surface well.

https://doi.org/10.1017/jfm.2020.281 Published online by Cambridge University Press

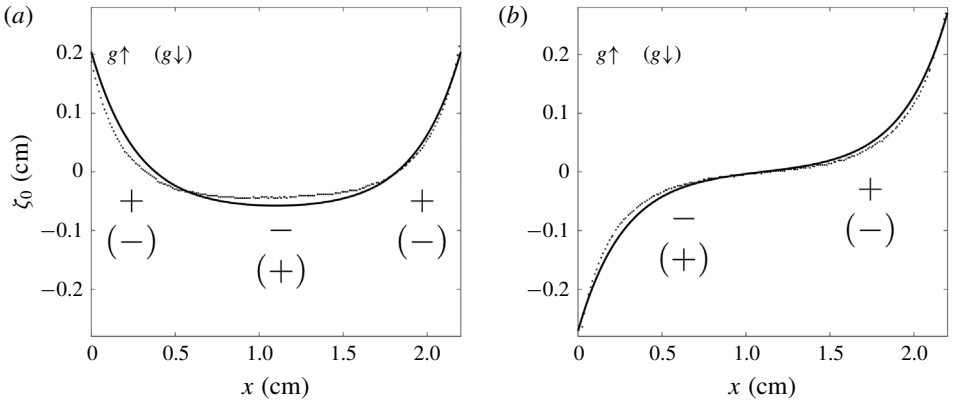


FIGURE 6. The zeroth-order meniscus solution ζ_0 (solid line) compared to the experimental measurement (dotted line) for (*a*) symmetric and (*b*) antisymmetric cases. The + and − signs represent the surplus and deficit of dynamical pressure p_d, respectively, that arises when the acceleration is changed by $a_0\omega\delta t$, where δt is a small time increment. The p_d distribution outside (inside) of the bracket is for the situation when g is increased (decreased).

3.1.2. *First-order solution*

At $O(\epsilon)$, the governing equations and boundary conditions become

$$\nabla^2\phi_1 = 0, \tag{3.13}$$

$$\partial_t\phi_1|_{z=0} + g_0\zeta_1 - \frac{\sigma}{\rho}\partial_{xx}^2\zeta_1 = -a_0\zeta_0\sin(\omega t), \tag{3.14}$$

$$\partial_z\phi_1|_{z=0} - \partial_t\zeta_1 = 0, \tag{3.15}$$

$$\phi_1|_{z=-\infty} = 0, \tag{3.16}$$

$$\partial_x\phi_1|_{x=0,L} = 0. \tag{3.17}$$

The first-order surface pressure balance (3.14) suggests a physical interpretation for the mechanism of the meniscus wave. Suppose that the system is initially at rest, so that $\zeta_1 = 0$, and the vertical acceleration increases by an amount $\delta g = a_0\omega\delta t$ over the background value g_0. At this instant, the dynamic pressure is

$$p_d = -\rho\partial_t\phi_1|_{z=0} = \rho\delta g\zeta_0, \tag{3.18}$$

so that there is an excess of dynamic pressure where $\zeta_0 > 0$ and a deficit where $\zeta_0 < 0$. In the symmetric case, this dynamic pressure perturbation will cause the free surface to fall in the centre of the cell and rise on the sides, leading to a wave with two nodes (figure 6*a*). For the antisymmetric case, the same process will cause the free surface to fall and rise on the left and right, respectively, sides of the cell, so the meniscus wave will have a single node (figure 6*b*). A decrease in the vertical acceleration will lead to the opposite pattern of dynamic pressure perturbations, resulting in the opposite surface deflection.

The solution that satisfies (3.13)–(3.17) takes the form

$$\phi_1 = \hat{\phi}_1\cos(\omega t) = \sum_{n=1}^{\infty} A_n \mathrm{e}^{k_n z}\cos(k_n x)\cos(\omega t), \tag{3.19}$$

https://doi.org/10.1017/jfm.2020.281 Published online by Cambridge University Press

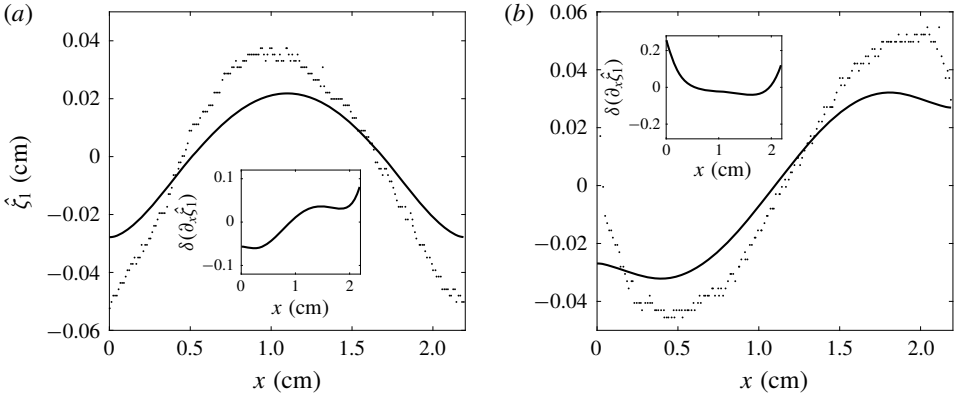


FIGURE 7. The first-order meniscus solutions $\hat{\zeta}_1$ (solid line) compared to the experimental measurements (dotted line) when $a_0 = 0.2g_0$ and $f_0 = 8$ Hz for (*a*) the symmetric and (*b*) the antisymmetric cases. The experimental $\hat{\zeta}_1$ are produced by subtracting the static surface profiles from the oscillating surface profiles captured during the slack phase. The insets show the difference between the theoretical first-order slope and the experimental first-order slope, $\delta(\partial_x\hat{\zeta}_1)$.

$$\zeta_1 = \hat{\zeta}_1 \sin(\omega t) = \sum_{n=1}^{\infty} \frac{A_n k_n}{\omega} \cos(k_n x) \sin(\omega t), \tag{3.20}$$

where the eigen-wavenumber $k_n = n\pi/L$ and coefficients A_n are given by

$$A_n = \frac{2\omega a_0}{\omega^2 - \omega_n^2} \frac{(-1)^n + s}{(m^2 + k_n^2)L}, \tag{3.21}$$

where

$$\omega_n^2 = g_0 k_n (1 + k_n^2 l_c^2) \tag{3.22}$$

is the (squared) natural frequency of a capillary–gravity wave with wavenumber k_n. Note that these wave modes (3.19) and (3.20) are not parametric resonance modes (Faraday modes), but ordinary resonance modes, since they have the same frequency as the forcing. The wave energy is concentrated around those n for which ω_n is close to ω. If $\omega = \omega_n$, for a given n, the capillary–gravity wave can travel integer multiples of the cell length during one forcing cycle. For a particular wave mode n and oscillation frequency ω, the mode amplitude A_n is also controlled by the distance between the boundary plates L. When the resonance condition $\omega = \omega_n(L)$ is satisfied by tuning L, the mode amplitude $A_n \to \infty$. The mode amplitude A_n goes to zero like L^{-1} as $L \to \infty$ and like L^4 as $L \to 0$. The forcing frequency $f_0 = 8$ Hz is approximately at the midpoint between two flat-surface resonant frequencies, $f_1 = 6.38$ Hz and $f_2 = 10.65$ Hz, for modes $n = 1$ and $n = 2$, respectively. If the equilibrium surface were flat, the amplitudes A_1 and A_2 would be comparable to each other. However, the (anti)symmetry of the equilibrium surface selects excitations with the corresponding (anti)symmetry: $A_1 = 0$ in the symmetric case and $A_2 = 0$ in the antisymmetric case (see (3.21)). The amplitude A_n decays like $O(n^{-5})$, so the series converges quickly. In figure 7, the infinite series is terminated at $n = 200$ to

https://doi.org/10.1017/jfm.2020.281 Published online by Cambridge University Press

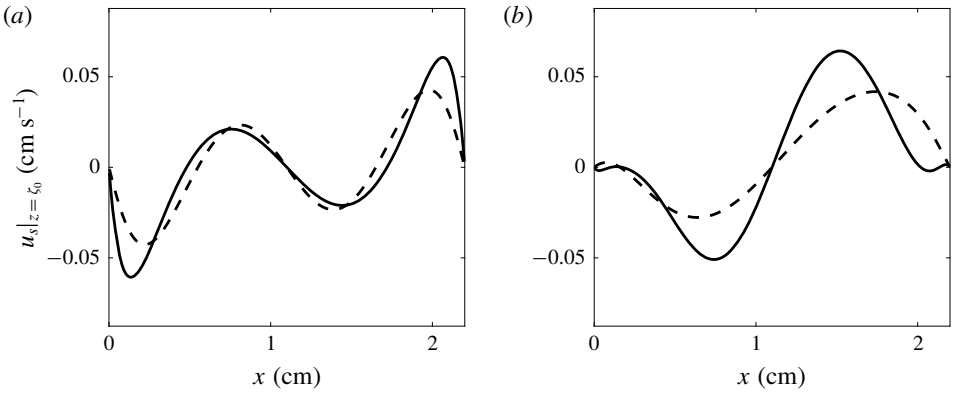


FIGURE 8. The streaming flow velocity along the free surface at $\varphi = \pi$, when $a_0 = 0.2g_0$ and $f_0 = 8$ Hz for (*a*) the symmetric and (*b*) the antisymmetric cases. The solid line is the result (3.26) truncated at $m + n = 200$, while the dashed line contains contributions from the gravest mode only.

produce the estimate of the meniscus wave amplitude $\hat{\zeta}_1$ for both symmetric and antisymmetric cases.

In figure 7, the experimental wave amplitudes are 67 % and 42 % larger than the theoretical values for the symmetric and antisymmetric cases, respectively. The linearized theory is inadequate to produce a more accurate result, because our basic scaling approximation $\partial_x(\zeta_0 + \zeta_1) \to 0$ is not satisfied since $\partial_x\zeta_0 \sim 1$ near the contact angle. The insets in figure 7 show the differences between the theoretical and experimental first-order slopes, $\delta(\partial_x\hat{\zeta}_1)$. The experimental slope is determined by fitting a fifth-order polynomial to the measured $\hat{\zeta}_1$ profile. We can see that $\delta(\partial_x\hat{\zeta}_1)$ is large near the contact line and zero near the centre of the cell.

The deviation between the experiment and theory may also due to the contact-line dynamics. In the theory, the contact line is assumed to be free-slipping with the liquid body. In the experimental measurement shown in figure 8, the amplitude of the oscillation near the contact line is larger (smaller) than predicted in the symmetric (antisymmetric) case. These interesting behaviours may contribute to the difference between the predicted and observed meniscus wave shapes. Nevertheless, a precise analytical model of the meniscus wave is not the main purpose of this work. In the next section, we will show that the meniscus wave solution obtained here is sufficient to explain the streaming circulation pattern formation.

3.2. *Streaming circulation*

In this section, we explain the secondary circulation pattern shown in figures 3 and 4. Firstly, we note that the surface appears to play a very important role in streaming circulation generation, since the number of secondary vortices doubles as the dominant mode number of the meniscus wave flow doubles. Moreover, the nodes of the meniscus wave are above upwelling flow, while the antinodes cap downwelling flows. The spatial relationships between the meniscus wave and the streaming flow indicate that the streaming flow is generated by the meniscus wave itself. This streaming flow affects the bulk through viscous momentum transfer, so as to generate a secondary circulation pattern.

The fluid surface was not frequently cleaned during the experiments, which leads to the build-up of surface contamination. The free surface is additionally contaminated

https://doi.org/10.1017/jfm.2020.281 Published online by Cambridge University Press

by a large number of seeding particles which form a membrane (see figure 2). Under these conditions, the free surface acts like a no-slip boundary (Henderson & Segur 2013; Moisy *et al.* 2018). We therefore treat the free surface as a vibrating solid when applying the streaming theory of Nicolás & Vega (2003).

3.2.1. *Streaming under the free surface*

Let the primary-flow-induced deflection normal to the unperturbed boundary, f, the primary-flow oscillation along the boundary, $u_\parallel$, and the tangential boundary-oscillation velocity, v^w, be written as

$$f = F\mathrm{e}^{\mathrm{i}\omega t} + \text{c.c.},$$
$$u_\parallel = U\mathrm{e}^{\mathrm{i}\omega t} + \text{c.c.},$$
$$v^w = U^w\mathrm{e}^{\mathrm{i}\omega t} + \text{c.c.},$$

where F is the normal oscillation amplitude and U^w is the tangential velocity amplitude of the boundary. With the present notation, the streaming velocity along a vibrating solid boundary in two dimensions is given by equations (6.2) of Nicolás & Vega (2003):

$$u^s_\perp = \partial_\tau(F^*U) + \text{c.c.}, \tag{3.23}$$

$$\begin{aligned} u^s_\parallel \;=\; & \kappa F^*(2U - 3U^w) - \mathrm{i}\omega F^*\partial_\tau F - \frac{3}{2\omega}[(U^* - U^{w*})\partial_\tau(U - U^w)] \\ & - \frac{\mathrm{i}}{\omega}[(3U - 5U^w)\partial_\tau U^*] - \frac{1}{\omega}(3U - U^w)\partial_\tau U^{w*} + \text{c.c.}, \end{aligned} \tag{3.24}$$

where ∂_τ is the derivative along the steady meniscus, $u^s_\perp$ and $u^s_\parallel$ are the streaming velocity normal and parallel to the steady meniscus, respectively, $\kappa \approx \partial^2_{xx}\zeta_0$ is the curvature of the unperturbed boundary, and U is the oscillation amplitude of the primary flow tangential to the steady free surface. According to our approximation $\partial_x\zeta_0 \to 0$, the tangential sliding of the unperturbed surface is negligible and we have $f \approx \zeta_1$ and $v^w \approx 0$.

The results (3.23) and (3.24) are independent of the oscillation phase, since the result is evaluated at the unperturbed boundary (equivalent to $\varphi = \pi$ in our case) and averaged over one period. For a standing wave, the normal deformation amplitude, f, and primary-flow velocity amplitude parallel to the free surface, $u_\parallel$, are given by

$$f \approx \hat{\zeta}_1 \sin(\omega t) = \frac{\hat{\zeta}_1}{2\mathrm{i}}(\mathrm{e}^{\mathrm{i}\omega t} - \mathrm{e}^{-\mathrm{i}\omega t}),$$
$$u_\parallel = u_\parallel \cos(\omega t) = \frac{\hat{u}_\parallel}{2}(\mathrm{e}^{\mathrm{i}\omega t} + \mathrm{e}^{-\mathrm{i}\omega t}),$$

where $\hat{\zeta}_1$ and $\hat{u}_\parallel$ are real functions, so that F and U are given by

$$F = \frac{\hat{\zeta}_1}{2i}, \quad U = \frac{\hat{u}_\parallel}{2}.$$

Substitution of F, U and U^w into (3.23) and (3.24) gives

$$\boldsymbol{u}_s|_{z=\zeta_0} = -\frac{3}{4\omega}\hat{u}_\parallel\partial_\tau\hat{u}_\parallel\hat{\boldsymbol{t}}, \tag{3.25}$$

https://doi.org/10.1017/jfm.2020.281 Published online by Cambridge University Press

where $\hat{\boldsymbol{t}}$ is the tangential unit vector along the meniscus. Note that, since the surface elevation is 90° out of phase with the flow field, the streaming flow normal to the meniscus surface $u^s_\perp = 0$. Moreover, the tangential streaming flow components proportional to the curvature κ and surface deformation F do not appear in the final result, which is of the same form as for an undeformable solid surface (Nicolás & Vega 2003). Although the term $\sim \kappa FU$ disappears in our system, its physical meaning is of interest. When there is a local curvature on the unperturbed free surface, the perpendicular deformation shrinks the curve element length in the curvature direction. Thus the boundary viscous stress does more (less) work at the phases when the surface curve element stretches (shrinks). For progressive waves, when the velocity oscillation along the surface is in phase with the normal deformation, the damping asymmetry within one period produces a net Eulerian flow. For standing waves, the deceleration of the velocity along the surface in both directions cancels each other to produce a zero periodical mean.

The tangential velocity at the meniscus when $\varphi = \pi$, i.e. $u_\parallel$, is obtained by linear extrapolation from $z = 0$ (see appendix B). By substituting the expression for $u_\parallel$ into (3.23), we find

$$\boldsymbol{u}_s|_{z=\zeta_0} = \left\{ -\frac{3}{4\omega} \sum_{n,m} A_n A_m (k_n + \zeta_0 k_n^2)(k_m + \zeta_0 k_m^2) \times \left[k_m - \frac{\rho g_0}{\sigma} (\zeta_0 - z^*) \right] \sin(k_n x) \cos(k_m x) + O(\partial_x \zeta_0) \right\} \hat{\boldsymbol{\imath}} + O(\partial_x \zeta_0) \hat{\boldsymbol{\jmath}}, \quad (3.26)$$

where $\hat{\boldsymbol{\imath}}$ and $\hat{\boldsymbol{\jmath}}$ are the horizontal and vertical unit vectors, respectively. From this result, we can see that the surface profile ζ_0 modifies the streaming velocity distribution. To be consistent with the scaling assumptions of the primary flow solution, we have neglected terms that are $O(\partial_x \zeta_0)$, which eliminates the vertical velocity along the meniscus.

The horizontal velocity along the meniscus, $u_s|_{z=\zeta_0}$, is shown in figure 8. In both cases, the gravest mode gives the largest contribution to the streaming velocity. With the contribution from the higher-order waves, the magnitude decreases in the symmetric case and increases in the antisymmetric case. The streaming velocity field is completely antisymmetric in the symmetric case, but lacks any definite symmetry in the antisymmetric case. This asymmetry can be understood by considering the fact that the velocity of deep-water waves decreases exponentially from the mean water depth (i.e. from $z = 0$). Since the steady liquid surface is higher on the hydrophilic side than on the hydrophobic side, the streaming velocity induced by the meniscus wave is also higher on the hydrophilic side. From (3.23), the wave-induced secondary flow inherits this strength distribution (see the schematic inset in figure 5), leading to an asymmetric streaming velocity distribution.

3.2.2. *Streaming near the lateral boundary*

The (flat) lateral solid boundaries are a limiting case of the deformable solid surface boundary where $\gamma = 0$ and $F = 0$. The previous results, equations (3.23) and (3.24), yield

$$\boldsymbol{u}_s|_{x=0,L} = -\frac{3}{4\omega} \hat{w}_1 \partial_z \hat{w}_1|_{x=0,L} \hat{\boldsymbol{t}}, \quad (3.27)$$

https://doi.org/10.1017/jfm.2020.281 Published online by Cambridge University Press

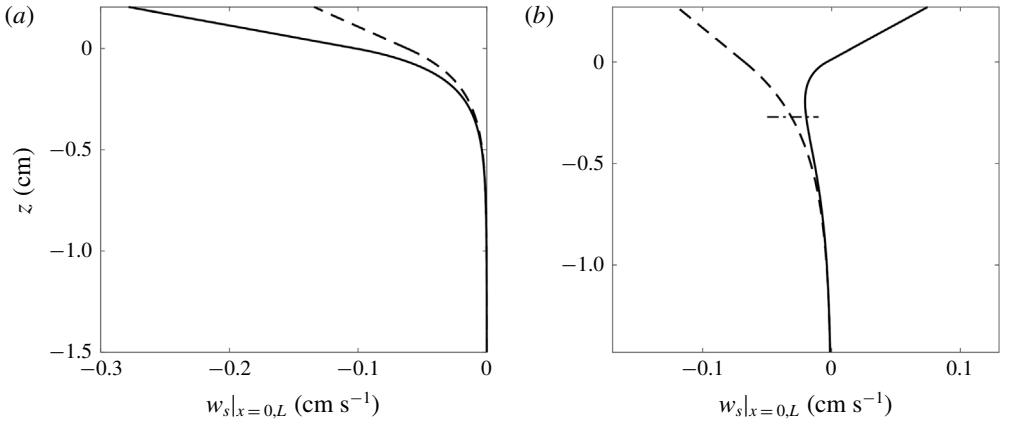


FIGURE 9. The streaming flow velocity distribution along the lateral boundary when $a_0 = 0.2g_0$, $f_0 = 8$ Hz for (*a*) the symmetric and (*b*) the antisymmetric cases. The solid line is the result (3.27) with the sum terminated at $m + n = 200$, while the dashed line contains contributions from the gravest mode only. The upper limit of the plot is the position of the liquid surface at hydrophilic boundary. The dash-dotted line in (*b*) shows the liquid surface position at the hydrophobic boundary.

where $\hat{w}_1|_{x=0,L} = \partial_z\phi_1|_{x=0,L}$ is the vertical velocity amplitude at the lateral boundary. Substituting the primary flow solution (3.19) into (3.27) and applying linear extrapolation (see appendix B), we find that

$$w_s|_{x=0,L} = \begin{cases} -\dfrac{3}{4\omega}\displaystyle\sum_{n,m} A_n A_m k_n k_m^2 (1 + zk_n)(1 + zk_m) & z \geqslant 0, \\ -\dfrac{3}{4\omega}\displaystyle\sum_{n,m} A_n A_m k_n k_m^2 \mathrm{e}^{(k_n + k_m)z} & z < 0. \end{cases} \tag{3.28}$$

This expression is valid for both symmetric and antisymmetric cases.

The vertical velocity distribution near the lateral boundary is shown in figure 9. The contribution from the gravest mode is similar in both the symmetric and antisymmetric cases. The two cases become distinct once higher-order contributions are included. The streaming velocity becomes stronger, but remains monotonic and negative in the symmetric case. In the antisymmetric case, the higher-order contributions weaken the streaming velocity and create a profile that is positive above $z = 0.013$ cm and has a negative extremum approximately 0.2 cm below the surface. This effect is due to phase modulation within the harmonic spectrum, A_n. All the A_n are positive in the symmetric case, so the components add constructively. In the antisymmetric case, A_1 is negative and the other A_n are positive, so interactions between the gravest and higher-order modes interfere destructively with the contributions from the wave self-interactions. Thus, in contrast to the monochromatic wave situation discussed by Périnet *et al.* (2017), the lateral boundary streaming velocity profile is affected by the relative phases of the component waves. In this experiment, the relative phases are controlled by the symmetry of static meniscus. Note that the streaming velocity is left–right symmetric in the symmetric case, but asymmetric in the antisymmetric case because the free surface on the hydrophobic side is lower than that on the hydrophilic side (see figure 9*b*).

https://doi.org/10.1017/jfm.2020.281 Published online by Cambridge University Press

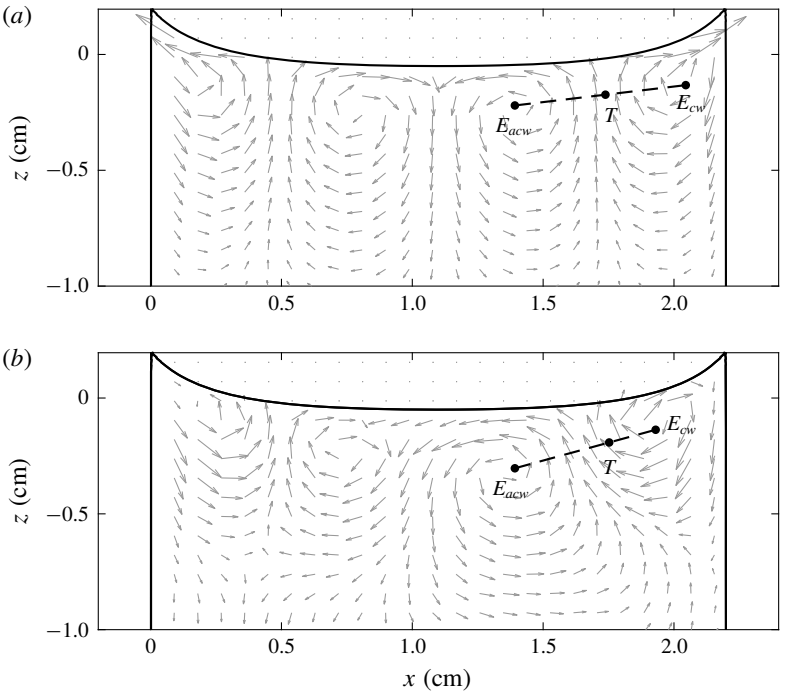


FIGURE 10. The secondary flow velocity beneath the oscillating meniscus for the symmetric case from (*a*) the numerical simulation and (*b*) the experiment. The forcing amplitude is $a_0 = 0.2g_0$ and the driving frequency is $f_0 = 8$ Hz. The phase chosen for simulation is $\varphi = \pi$. The centre of the anticlockwise (clockwise) circulation is denoted by E_{acw} (E_{cw}). The point where the velocity perpendicular to the line connecting E_{acw} and E_{cw} is maximal, denoting a transition between anticlockwise and clockwise vortices, is given by T.

3.2.3. *Numerical simulation of streaming circulation*

Following Périnet *et al.* (2017), we obtain the secondary flow in the bulk by using the steady streaming velocity profile as boundary conditions for the laminar flow solver in COMSOL Multiphysics® using a fixed (i.e. not deforming) domain at $\varphi = \pi$. Taking the characteristic velocity U to be the r.m.s. velocity of the surface streaming velocity distribution, and the characteristic length to be the cell width L, the maximum Reynolds number is 24 for streaming circulation. We simulate the steady secondary circulation at seven different oscillation amplitudes with the driving frequency $f_0 = 8$ Hz.

The steady secondary circulation induced by the oscillation at $a_0 = 0.2g_0$ is shown in figures 10 and 11. A nonlinear transformation is applied to the magnitude of the flow vectors to better visualize their direction. The numerical simulation successfully reproduces the four-vortex circulation structure in the symmetric case and the dipole circulation structure in the antisymmetric case. The scalings for the r.m.s. speed, v_{rms}, and the symmetry parameter, γ, from the numerical simulations are shown in figure 5. The numerical solutions follow the same scaling law, $v_{rms} \sim (a_0/g_0)^2$, as the experiments, but the value of the r.m.s. speed is approximately one order of magnitude smaller (figure 5*a*). The error in the first-order solution (see figure 7) accounts for

https://doi.org/10.1017/jfm.2020.281 Published online by Cambridge University Press

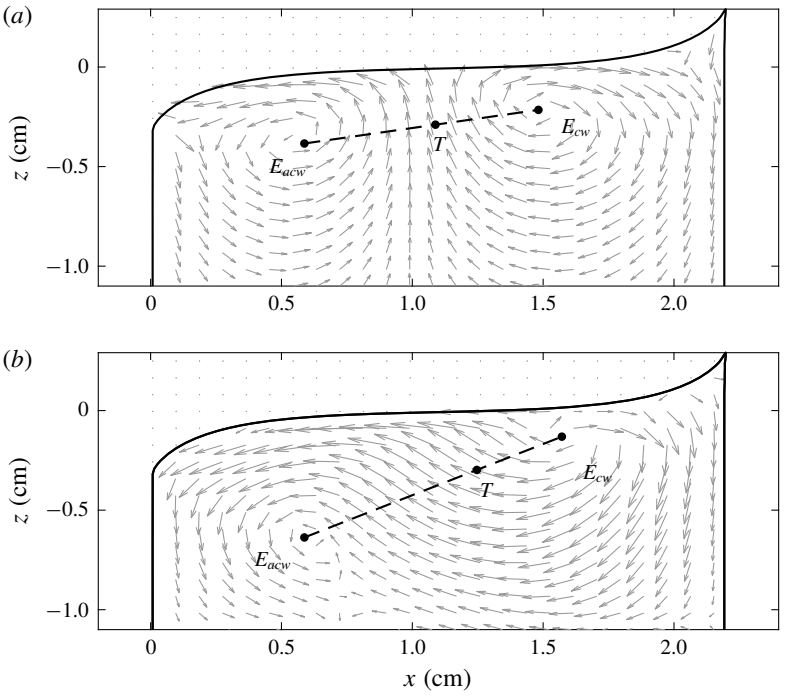


FIGURE 11. The secondary flow velocity beneath the oscillating meniscus for the antisymmetric case from (*a*) the numerical simulation and (*b*) the experiment. The forcing amplitude is $a_0 = 0.2g_0$ and the driving frequency is $f_0 = 8$ Hz. The phase chosen for simulation is $\varphi = \pi$. The centre of the anticlockwise (clockwise) circulation is denoted by E_{acw} (E_{cw}). The point where the velocity perpendicular to the line connecting E_{acw} and E_{cw} is maximal, denoting a transition between anticlockwise and clockwise vortices, is given by T.

approximately 15 % of the total error in both symmetric and antisymmetric cases; the remaining error must be due to other effects.

In order to determine the source of this additional error, we quantify the rotation speed of the eddies to gain additional insight into the streaming circulation structure and the energy distribution in the bulk. The rotation speed of each vortex is measured along a section connecting the centre of a anticlockwise circulation, E_{acw}, and the adjacent clockwise circulation, E_{cw}. The two vortices are separated by the point T where the velocity perpendicular to $E_{acw}E_{cw}$ is maximal. The radii and speed of the vortices are then defined by

$$r_{acw} = \Delta(E_{acw}T), \quad v_{acw} = \frac{1}{r_{acw}} \int_{E_{acw}\to T} v_n \, \mathrm{d}l, \tag{3.29a,b}$$

$$r_{cw} = \Delta(E_{cw}T), \quad v_{cw} = \frac{1}{r_{cw}} \int_{T\to E_{cw}} v_n \, \mathrm{d}l, \tag{3.30a,b}$$

where $\Delta(E_{acw}T)$ and $\Delta(E_{cw}T)$ are the lengths of the lines connecting E_{acw} and E_{cw}, respectively, to T, and v_n is the velocity perpendicular to $E_{acw}E_{cw}$. The resulting speed and radii for the different cases are shown in table 1.

https://doi.org/10.1017/jfm.2020.281 Published online by Cambridge University Press

Cases	r_{acw} (cm)	r_{cw} (cm)	v_{acw} (cm s^{-1})	v_{cw} (cm s^{-1})
Symmetric simulation	0.35	0.31	4.3×10^{-3}	6.2×10^{-3}
Symmetric experiment	0.38	0.19	2.7×10^{-2}	3.3×10^{-2}
Antisymmetric simulation	0.51	0.40	1.2×10^{-2}	1.3×10^{-2}
Antisymmetric experiment	0.74	0.37	5.1×10^{-2}	5.4×10^{-2}

TABLE 1. Radii and speed for vortices from the simulations and experiments.

We find that r_{cw} is always smaller than r_{acw}, while v_{cw} is always larger than v_{acw}. This means that the vortices near the hydrophilic boundary are smaller and relatively faster in both the symmetric and antisymmetric cases. The speed of the vortices is of the order 10^{-3}–10^{-2} cm s^{-1} for both the experiments and simulations. Consistent with the result from the v_{rms} calculation, the experiment gives a result approximately five or six times larger than the simulation. The difference between simulation and experiment is slightly larger for the clockwise vortex than for the anticlockwise vortex. This suggests that our model fails to completely capture the physics of the hydrophilic boundary. The impact of three-dimensional (3-D) effects on the circulation is estimated in appendix A by calculating the compression rate. We find a significant secondary flow convergence in the y direction near the hydrophilic boundary (figure 12). The convergence near the hydrophilic boundary induces a downwelling jet on the observational plane and makes a significant contribution to the secondary circulation near the hydrophilic boundary. This effect explains the significant symmetry loss in the antisymmetric case and may account for the remaining discrepancy between the simulations and experiments.

The numerical experiments were repeated with the surface streaming condition replaced by a free-slip boundary. The four-vortex structure is lost in the symmetric case and the kinetic energy drops by an order of magnitude in both cases. These results demonstrate that the free surface is a significant source of momentum for the secondary circulation and is important for determining its qualitative structure.

4. Conclusion

We observe the streaming circulation excited by standing capillary–gravity waves using PIV. It is found that the structure of the streaming circulation is controlled by the static meniscus shape. A semi-analytical theory is developed which explains the streaming pattern.

The experiment is designed to inhibit Faraday waves, so the streaming circulation is driven by meniscus waves, rather than by Faraday waves, as reported previously (Gordillo & Mujica 2014; Périnet *et al.* 2017). Two different linear meniscus wave modes in the x direction are generated by choosing the boundary wettability conditions. In experiments with hydrophilic–hydrophilic boundary conditions, the static meniscus is symmetric and the gravest meniscus wave mode has two nodes. In experiments with hydrophobic–hydrophilic boundary conditions, however, the static meniscus is antisymmetric and the gravest mode has a single node. The experimentally measured free-surface profiles are used to develop an analytical model for the linear meniscus waves. This model reveals that meniscus waves are standing capillary–gravity waves with a spectrum determined by the Fourier spectrum of the static meniscus profile. The analytical results give the correct dominant mode number and structure, and predict the wave amplitude within an order of magnitude of the experimental results.

https://doi.org/10.1017/jfm.2020.281 Published online by Cambridge University Press

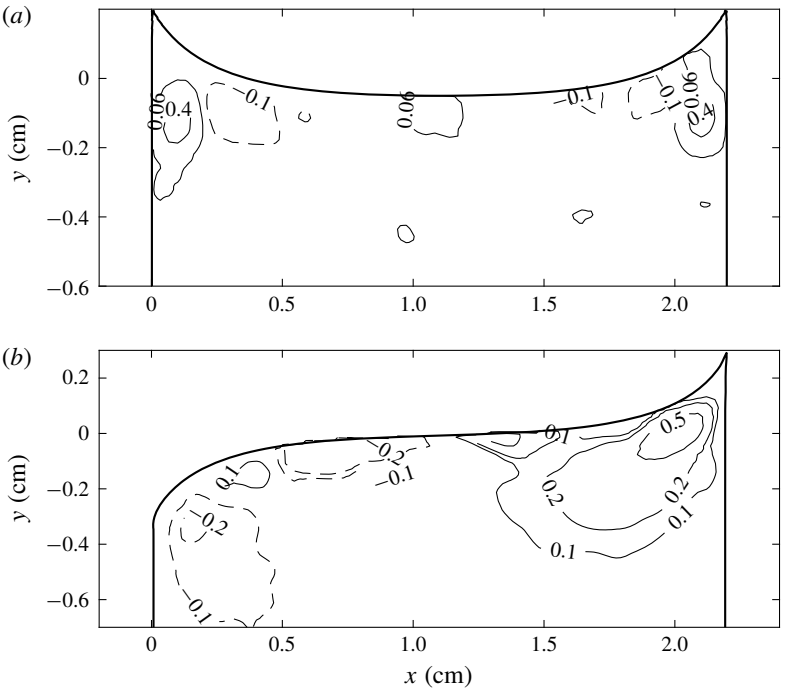


FIGURE 12. Divergence of the 2-D streaming flow at $a_0/g_0 = 0.2$ and $f_0 = 8$ Hz for (a) the symmetric and (b) the antisymmetric cases. Negative contours are dashed. The phase $\varphi = 9/10\pi$ ($\varphi = 13/10\pi$) for the symmetric (antisymmetric) case.

The secondary circulation induced by the meniscus wave is observed by broadcasting PIV images stroboscopically. The secondary flow originates from the Stokes boundary layer under a contaminated free surface, where the Reynolds stress induced by the meniscus wave is balanced by the viscous stress. The meniscus wave produces a four-vortex structure in the symmetric case, while a vortex dipole is generated in the antisymmetric case. The r.m.s. circulation speed, v_{rms}, scales like the square of the forcing amplitude (i.e. $v_{rms} \sim (a_0/g_0)^2$), regardless of the static surface profile. For $a_0 = 0.2g_0$, the secondary circulation has a speed of 10^{-3}–10^{-2} cm s^{-1}. In the symmetric case, the secondary flow retains a high degree of left–right symmetry as the forcing amplitude is increased. For the antisymmetric case, the flow symmetry is broken; such an asymmetry comes from the exponential decay of the velocity from $z = 0$, so the places with higher mean elevation have greater velocity under them. As a result, the antisymmetric surface profile gives rise to the asymmetry of streaming circulation.

Using the strategy suggested by Nicolás & Vega (2003) and Gordillo & Mujica (2014), we simulate the secondary flow by calculating the streaming velocities along the free surface and lateral boundaries and use these as boundary conditions for a laminar model. The simulated secondary flows have the same spatial structures, obey the same speed scaling, and have similar symmetry properties as the experimental flows. The theoretical model reveals that the secondary flow is shaped by the entire wave spectrum rather than by a monochromatic wave, as has been studied extensively in the previous literature. In particular, the relative phases of harmonic modes significantly affect the resulting streaming velocity distribution.

https://doi.org/10.1017/jfm.2020.281 Published online by Cambridge University Press

Several limitations of this analysis should be re-emphasized. First, although the theory successfully captures the spatial structure of the meniscus wave, the solution is inaccurate in the region near the contact line because we have assumed that the surface slope is small, whereas $\partial_x\zeta \sim 1$ near the contact line. Furthermore, the physics of the contact line and dynamic contact angle at microscopic scales were not considered (c.f. Yi, Ding & Spelt 2014). Second, the theory focuses on 2-D dynamics, since the experiment only measures a single cross-section of the flow field. However, 3-D effects play some role in the secondary circulation, but we lack the data to fully account for these effects. For these reasons, the agreement between the theory and experiment is not fully quantitative. In particular, the amplitudes of the meniscus waves and the strengths of the secondary circulations are underestimated. Based on the limitations of the present study, the streaming circulation inside the wedge in the vicinity of the contact line would be an interesting point for further research.

Acknowledgements

We are grateful to J. Yu, R. Wilson and D.-P. Wang for stimulating discussions. We also thank J.-Q. Shi and Z. Chen for their participation in the early stage of the experiment. This work was supported by the National Science Foundation of China through grant nos 11572230 and 11772235, and a NSFC/RGC Joint Grant no. 11561161004.

Declaration of interests

The authors report no conflict of interest.

Supplementary movies

Supplementary movies that show the streaming circulations produced by an oscillating meniscus (symmetric/antisymmetric, $a_0 = 0.2g_0$, $f_0 = 8$ Hz) are available at https://doi.org/10.1017/jfm.2020.281.

Appendix A. Estimates of 3-D effects

To estimate how motion in the y direction affects the motion in the x–z plane, we compute the 2-D divergence rate, defined as

$$\partial_x u + \partial_z w.$$

The hydrophilic boundaries are regions of strong divergence, while the hydrophobic boundary is associated with less intense, but larger-scale, convergence (figure 12). In the symmetric case, the divergence zones are flanked by weaker convergence zones, which indicate flow in the plane directed away from the boundaries (i.e. from the divergence to the convergence zones). The arrangement of convergence and divergence zones in the antisymmetric case implies a more broadly distributed flow from the right (hydrophilic) boundary to the left (hydrophobic) boundary. The divergent flow contributes to the streaming circulation in both cases and enhances the asymmetry of the antisymmetric case. Since our experiment only imaged in midplane of the fluid cell, we lack the data to determine the cause of this 3-D circulation. Further experiments and 3-D analysis should be designed to examine this 3-D secondary flow.

https://doi.org/10.1017/jfm.2020.281 Published online by Cambridge University Press

Appendix B. Faraday threshold

This experiment focuses on streaming driven by natural cavity standing wave modes, rather than a Faraday wave excited by parametric instability. The experiment is therefore conducted in a stable zone of the Faraday instability. Here, we demonstrate that the experiment is indeed within a stable zone. The time-dependent surface deformation, ζ_{kl}, of a linear standing wave mode in a rectangular channel is

$$\zeta_{kl} = a_{kl}(t)\cos\left(\frac{\pi k x}{L_x}\right)\cos\left(\frac{\pi l y}{L_y}\right), \tag{B 1}$$

where (k, l) are the mode numbers in the x and y directions, respectively, and a_{kl} is the mode amplitude. From Benjamin & Ursell (1954), the mode amplitude a_{kl} evolves according to the differential equation

$$\frac{\mathrm{d}^2 a_{kl}}{\mathrm{d}T^2} + [p_{kl} - 2q_{kl}\cos(2T)]a_{kl} = 0, \tag{B 2}$$

which is known as Mathieu's equation (Abramowitz & Stegun 1965). In this equation, $T = \frac{1}{2}\omega t$ is dimensionless time and the parameters p_{kl} and q_{kl} are

$$p_{kl} = \frac{4K_{kl}\tanh(K_{kl}h)}{\omega^2}\left(g_0 + \frac{\sigma}{\rho}K_{kl}^2\right), \tag{B 3}$$

$$q_{kl} = 2K_{kl}a_0\frac{\tanh(K_{kl}h)}{\omega^2}, \tag{B 4}$$

where

$$K_{kl}^2 = \frac{\pi^2 k^2}{L_x^2} + \frac{\pi^2 l^2}{L_y^2} \tag{B 5}$$

is the total wavenumber. The mathematical character of Mathieu's equation is such that some modes grow exponentially in time while others – in the stable zones – decay exponentially. The decaying modes are not observable in this experiment, since their amplitudes rapidly become too small to measure. For the forcing frequency $f_0 = 8$ Hz,

$$p_{10} \approx 2.5, \quad p_{20} \approx 7.1,$$

and the associated instability thresholds are $q_{10}^T \approx 2.6$ and $q_{20}^T \approx 4.4$ (Abramowitz & Stegun 1965). The corresponding threshold forcing accelerations are $a_{10}^T \approx 2.36g_0$ and $a_{20}^T \approx 2.01g_0$. In our experiment, we chose $a_0 \leqslant 0.36g_0$, which is well below the Faraday instability threshold and the observed (1, 0) and (2, 0) modes are therefore ordinary resonant modes.

Appendix C. Extrapolation method

In this section, we describe the extrapolation method used to calculate the streaming velocity distribution along the meniscus at $z = \zeta_0(x)$. Instead of extrapolating the secondary flow velocity directly, we extrapolate the primary flow (i.e. the linear meniscus wave) velocity to ensure continuity of the first-order velocity. The primary flow velocities extrapolated to the static meniscus are

$$u_1|_{z=\zeta_0} \approx u_1|_{z=0} + \left.\frac{\partial u_1}{\partial z}\right|_{z=0}\zeta_0 = -\cos\omega t\sum_n^{\infty} A_n k_n[1 + k_n\zeta_0]\sin k_n x, \tag{C 1}$$

https://doi.org/10.1017/jfm.2020.281 Published online by Cambridge University Press

$$w_1|_{z=\zeta_0} \approx w_1|_{z=0} + \left.\frac{\partial w_1}{\partial z}\right|_{z=0} \zeta_0 = \cos\omega t \sum_n^{\infty} A_n k_n [1 + k_n\zeta_0] \cos k_n x. \tag{C 2}$$

The velocity tangent to the free surface is the projection of (C 1) and (C 2) onto the tangential direction $\hat{\boldsymbol{t}}$:

$$\begin{aligned} u_\parallel &= (u_1, w_1)|_{z=\zeta_0} \cdot \hat{\boldsymbol{t}} \\ &= -\cos\omega t \sum_n^{\infty} A_n k_n \frac{1 + k_n\zeta_0}{[1 + (\partial_x\zeta_0)^2]^{1/2}} (\sin k_n x - \partial_x\zeta_0 \cos k_n x) \\ &\approx -\cos\omega t \sum_n^{\infty} A_n k_n (1 + k_n\zeta_0) \sin k_n x, \end{aligned} \tag{C 3}$$

where we have used the fact that $\partial_x\zeta_0 \sim O(\epsilon)$ in the last step. Again using the fact that $\partial_x\zeta_0 \sim O(\epsilon)$, we estimate the tangential derivative of the tangential velocity as

$$\partial_\tau u_\parallel \approx \partial_x u_\parallel \approx \cos\omega t \sum_n^{\infty} A_n k_n (1 + k_n\zeta_0)(\partial_{xx}^2\zeta_0 - k_n) \cos k_n x. \tag{C 4}$$

Substituting (C 3) and (C 4) into (3.23), we find that the streaming velocity along the free surface is

$$\begin{aligned} \boldsymbol{u_s} &= (u_s, w_s) = -\frac{3}{4\omega}\tilde{u}_\parallel \partial_\tau \tilde{u}_\parallel \hat{\boldsymbol{t}} \\ &\approx -\frac{3}{4\omega}\hat{\boldsymbol{i}} \sum_{n,m}^{\infty} A_n A_m k_m k_n (1 + k_m\zeta_0)(1 + k_n\zeta_0)(k_n - \partial_{xx}^2\zeta_0) \sin k_m x \cos k_n x, \end{aligned} \tag{C 5}$$

where we have used the facts that $\hat{\boldsymbol{t}} \cdot \hat{\boldsymbol{i}} \approx 1$, and $\hat{\boldsymbol{t}} \cdot \hat{\boldsymbol{k}} \approx 0$. The process is similar for extrapolation on the lateral boundaries. When $z \leqslant 0$, the streaming velocity is the same as for a flat surface. When $z > 0$, the vertical velocity at arbitrary position z' is estimated by

$$w_1|_{z=z'} \approx w_1|_{z=0} + \left.\frac{\partial w_1}{\partial z}\right|_{z=0} z'. \tag{C 6}$$

It should be mentioned that the extrapolation for the velocity does not converge for arbitrary order of the Taylor expansion. As A_n converges like n^{-5}, the extrapolation polynomial in (C 1) and (C 2) should be no higher than the second order.

Appendix D. Derivation of the boundary layer streaming velocity

In this section, we provide a detailed derivation of a 2-D boundary layer streaming velocity under a vibrating solid boundary with a curved unperturbed state, i.e. equations (3.23) and (3.24), using the method of Nicolás & Vega (2003). The derivation in this appendix uses dimensionless variables to maintain consistency with Nicolás & Vega (2003). The duplicated symbols t, τ, f, U and F share the same physical meaning as those in the rest of the paper, but do not have units. The tangential oscillation of the boundary is not considered in this derivation.

https://doi.org/10.1017/jfm.2020.281 Published online by Cambridge University Press

D.1. *Governing equation*

We scale lengths by the capillary length l_c, velocity by ωl_c and pressure by $\rho\omega^2 l_c^2$. The non-dimensional 2-D Navier–Stokes and continuity equations transformed into a curvilinear orthogonal coordinate frame, (τ, ξ), following the unperturbed boundary are

$$\partial_t\tilde{v} + \tilde{v}\partial_\tau\tilde{v} + \tilde{w}\partial_\xi\tilde{v} - \tilde{w}\kappa\tilde{v} = -(1+\xi\kappa)\partial_\tau p + R^{-1}\partial^2_{\xi\xi}\tilde{v}, \tag{D 1}$$

$$\partial_t\tilde{w} + \tilde{v}\partial_\tau\tilde{w} + \tilde{w}\partial_\xi\tilde{w} + \tilde{v}\kappa\tilde{v} = -\partial_\xi p + R^{-1}\partial^2_{\xi\xi}\tilde{w}, \tag{D 2}$$

$$\partial_\tau\tilde{v} + \partial_\xi\tilde{w} - \kappa\tilde{w} = 0, \tag{D 3}$$

where the velocity in curvilinear coordinates is denoted by $(\tilde{u}, \tilde{v})$ and R is the Reynolds number, defined by $R = \omega l_c^2/\nu$. The small parameter used for the asymptotic expansion is $\epsilon = a_0/(\omega^2 l_c)$. The basic asymptotic assumptions of Nicolás & Vega (2003), namely that $R \gg 1$ and $\epsilon \ll 1$, are satisfied by our experiments.

To study the boundary layer flow inside the oscillatory boundary layer, equations (D 1)–(D 3) are further rescaled by

$$\tau^* = \tau, \quad \tilde{w}^* = \tilde{w} - \partial_t f - \tilde{v}\partial_\tau f, \quad \eta = R^{1/2}(\xi - f). \tag{D 4a–c}$$

The boundary layer thickness is $O(R^{-1/2})$, the tangential velocity $\tilde{v}$ and surface deformation f are $O(\epsilon)$, and the normal velocity $\tilde{w}$ is $O(\epsilon R^{-1/2} + \epsilon^2)$. Eliminating terms smaller than $O(\epsilon R^{-1/2} + \epsilon^2)$, the equations for a boundary layer on an oscillating solid boundary are

$$\partial_t\tilde{v} + \tilde{v}\partial_\tau\tilde{v} + R^{1/2}[(\tilde{w}^* + \tilde{v}\partial_\tau f)\partial_\eta\tilde{v} - \partial_\eta p\partial_\tau f] - \kappa\partial_t f\tilde{v} + \partial_\tau p + (f + R^{-1/2}\eta)\kappa\partial_\tau p - \partial^2_{\eta\eta}\tilde{v} = 0, \tag{D 5}$$

$$\partial_\eta p + R^{-1/2}(\partial^2_{tt} f - \partial^2_{\eta\eta}\tilde{w}^*) = 0, \tag{D 6}$$

$$\partial_\eta\tilde{w}^* + R^{-1/2}(\partial_\tau\tilde{v} - \kappa\partial_t f) = 0. \tag{D 7}$$

These are identical to the 2-D form of equations (5.1)–(5.4) in Nicolás & Vega (2003). For notational convenience, we drop the * decorating t^* and τ^* in (D 5)–(D 7). The boundary condition at $\eta = 0$ is

$$\tilde{w}^* = 0, \quad \tilde{v} = 0. \tag{D 8a,b}$$

The connection condition at $\eta \to \infty$ depends on the form of the equation at each scale.

D.2. *Perturbation solution*

Consider the perturbation expansion

$$f = \epsilon F e^{it} + \text{c.c.} + \cdots, \tag{D 9}$$

$$\tilde{v} = \epsilon(V_0 + R^{-1/2}V_1)e^{it} + \text{c.c.} + \epsilon^2(v^s + \text{O.T.}) + \cdots, \tag{D 10}$$

$$\tilde{w}^* = \epsilon R^{-1/2}W_1 e^{it} + \text{c.c.} + \epsilon^2(w^s + \text{O.T.}) + \cdots, \tag{D 11}$$

$$p = \epsilon(P_0 + R^{-1/2}P_1)e^{it} + \text{c.c.} + \epsilon^2(p^s + \text{O.T.}) + \cdots. \tag{D 12}$$

Here F is the deformation amplitude perpendicular to the liquid surface, V and W are the tangential and normal velocity amplitudes, respectively, and P is the pressure amplitude. The numbers in the subscripts represent the order number. The

https://doi.org/10.1017/jfm.2020.281 Published online by Cambridge University Press

time-independent streaming components of the tangential velocity, normal velocity and pressure are v^s, w^s and p^s, respectively; and O.T. stands for oscillation terms with zero average. We substitute these expansions into (D 5)–(D 7) and solve at order $O(\epsilon)$, $O(\epsilon/\sqrt{R})$ and $O(\epsilon^2)$ sequentially.

The solution at $O(\epsilon)$ order represents a typical Stokes boundary layer:

$$P_0 = P_0^0(\tau), \tag{D 13}$$

$$V_0 = U(\tau)(1 - \mathrm{e}^{\sqrt{\mathrm{i}}\eta}), \tag{D 14}$$

where we take the branch of the square root where $\sqrt{\mathrm{i}} = -(1+\mathrm{i})/\sqrt{2}$. The pressure gradient along the free surface is balanced by the outer (potential) flow acceleration, so we have

$$\partial_\tau P_0^0 = -\mathrm{i}U, \tag{D 15}$$

where U is the outer flow amplitude. The connection condition is $\partial_\eta V_0|_{\eta\to\infty} = 0$.

At order $O(\epsilon/\sqrt{R})$, the solution is

$$P_1 = F\eta + P_1^0(\tau), \tag{D 16}$$

$$V_1 = -\mathrm{i}\partial_\tau P_1^0(1 + \mathrm{e}^{\sqrt{\mathrm{i}}\eta}) + H\eta, \tag{D 17}$$

$$W_1 = (\mathrm{i}\kappa F - \partial_\tau U)\eta + (\mathrm{e}^{\sqrt{\mathrm{i}}\eta} - 1)\frac{\partial_\tau U}{\sqrt{\mathrm{i}}}, \tag{D 18}$$

where $H = \kappa U + \mathrm{i}\partial_\tau F$ and $P_1^0(\tau)$ is an arbitrary function.

At order $O(\epsilon^2)$, the streaming pressure p^s and normal velocity w^s are

$$p^s = p^{s0}(\tau), \tag{D 19}$$

$$w^s = 0, \tag{D 20}$$

where $p^{s0}(\tau)$ is also an arbitrary function to be determined. The horizontal streaming velocity can be integrated under the condition $\partial_\eta v^s|_{\eta\to\infty} = 0$ and has the limit at $\eta \to \infty$ of

$$v^s|_{\eta\to\infty} = 3\kappa F^* U - \tfrac{3}{2}[U\partial_\tau U^* + \mathrm{i}U\partial_\tau U^*] + \text{c.c.} \tag{D 21}$$

This results in the boundary layer flow at $\eta \to \infty$ and holds for the outer flow at the unperturbed boundary at $\xi = f$. The streaming pressure p^s is chosen to cancel the singularity in the integration of v^s and is

$$p^s = |F|^2 - |U|^2 + p^{s0}, \tag{D 22}$$

where p^{s0} is independent of η or τ.

D.3. *Streaming velocity at the unperturbed boundary*

Since the solution (D 21) is only valid at $\xi = f$, we must extrapolate the result onto the unperturbed boundary at $\xi = 0$ during the numerical simulation. A first-order Taylor expansion from $\xi = f$ gives

$$\tilde{v}(\xi) = \tilde{v}|_{\xi=f} + \partial_\xi \tilde{v}|_{\xi=f}(\xi - f) + \cdots, \tag{D 23}$$

$$\tilde{w}(\xi) = \tilde{w}|_{\xi=f} + \partial_\xi \tilde{w}|_{\xi=f}(\xi - f) + \cdots. \tag{D 24}$$

https://doi.org/10.1017/jfm.2020.281 Published online by Cambridge University Press

The matching condition is that the outer flow should be consistent with the boundary layer flow at $R \to \infty$ and $\eta \to \infty$, so we have

$$f = \epsilon F \mathrm{e}^{\mathrm{i}t} + \text{c.c.} + \cdots, \tag{D 25}$$

$$\begin{aligned} \tilde{v} &= \epsilon V_0|_{\eta\to\infty}\mathrm{e}^{\mathrm{i}t} + \text{c.c.} + \epsilon^2(v^s|_{\eta\to\infty} + \text{O.T.}) + \cdots \\ &= \epsilon U \mathrm{e}^{\mathrm{i}t} + \text{c.c.} + \epsilon^2(v^s|_{\xi=f} + \text{O.T.}) + \cdots, \end{aligned} \tag{D 26}$$

$$\begin{aligned} \tilde{w} &= \partial_t f + \tilde{v}\partial_\tau f + \cdots \\ &= \epsilon \mathrm{i} F \mathrm{e}^{\mathrm{i}t} + \text{c.c.} + \epsilon^2(U\partial_\tau F^* + \text{c.c.} + \text{O.T.}) + \cdots \\ &= \epsilon \mathrm{i} F \mathrm{e}^{\mathrm{i}t} + \text{c.c.} + \epsilon^2(w^s|_{\xi=f} + \text{O.T.}) + \cdots. \end{aligned} \tag{D 27}$$

Using the expansion $\partial_\xi \tilde{v} = \kappa\tilde{v} + \partial_\tau \tilde{w}$, and the continuity equation $\partial_\tau \tilde{v} + \partial_\xi \tilde{w} - \kappa\tilde{w} = 0$, we find

$$\partial_\xi \tilde{v} = \epsilon[(\kappa U + \mathrm{i}\partial_\tau F)\mathrm{e}^{\mathrm{i}t} + \text{c.c.}] + \cdots, \tag{D 28}$$

$$\partial_\xi \tilde{w} = \epsilon[(\mathrm{i}\kappa F - \partial_\tau U)\mathrm{e}^{\mathrm{i}t} + \text{c.c.}] + \cdots. \tag{D 29}$$

Substituting (D 21) and (D 25)–(D 29) into (D 23) and (D 24) and averaging over an oscillation period results in

$$\begin{aligned} v^s|_{\xi=0} &= v^s|_{\eta\to\infty} - \overline{\partial_\xi|_{\xi=f}\tilde{v}f} \\ &= \left[3\kappa F^* U - \tfrac{3}{2}(U\partial_\tau U^* + \mathrm{i}U\partial_\tau U^*)\right] - (\kappa F^* U + \mathrm{i}F^*\partial_\tau F) + \text{c.c.} \\ &= 2\kappa F^* U - \tfrac{3}{2}(U\partial_\tau U^* + \mathrm{i}U\partial_\tau U^*) - \mathrm{i}F^*\partial_\tau F + \text{c.c.} \end{aligned} \tag{D 30}$$

and

$$\begin{aligned} w^s|_{\xi=0} &= w^s|_{\eta\to\infty} - \overline{\partial_\xi|_{\xi=f}\tilde{w}f} \\ &= U\partial_\tau F^* + F^*\partial_\tau U - \mathrm{i}\kappa F^* F + \text{c.c.} \\ &= \partial_\tau(UF^*) + \text{c.c.}, \end{aligned} \tag{D 31}$$

where an overbar denotes a time average. Equations (D 30) and (D 31) are 2-D versions of equations (6.2) and (6.3) in Nicolás & Vega (2003).

REFERENCES

Abramowitz, M. & Stegun, I. A. 1965 *Handbook of Mathematical Functions: With Formulas, Graphs, and Mathematical Tables*. Dover.

Antkowiak, A., Bremond, N., Le Dizès, S. & Villermaux, E. 2007 Short-term dynamics of a density interface following an impact. *J. Fluid Mech.* **577**, 241–250.

Batchelor, G. K. 2000 *An Introduction to Fluid Dynamics*. Cambridge University Press.

Benjamin, T. B. & Ursell, F. 1954 The stability of the plane free surface of a liquid in vertical periodic motion. *Proc. R. Soc. Lond.* A **225**, 505–515.

Carrión, L. M., Herrada, M. A., Montanero, J. M. & Vega, J. M. 2017 Mean flow produced by small-amplitude vibrations of a liquid bridge with its free surface covered with an insoluble surfactant. *Phys. Rev.* E **96**, 033101.

Chen, P., Luo, Z., Güven, S., Tasoglu, S., Ganesan, A. V., Weng, A. & Demirci, U. 2014 Microscale assembly directed by liquid-based template. *Adv. Mater.* **26**, 5936–5941.

Douady, S. 1990 Experimental study of the Faraday instability. *J. Fluid Mech.* **221**, 383–409.

https://doi.org/10.1017/jfm.2020.281 Published online by Cambridge University Press

FARADAY, M. 1831 XVII. On a peculiar class of acoustical figures; and on certain forms assumed by groups of particles upon vibrating elastic surfaces. *Proc. R. Soc. Lond.* A **121**, 299–340.

FRANCOIS, N., XIA, H., PUNZMANN, H., FONTANA, P. W. & SHATS, M. 2017 Wave-based liquid-interface metamaterials. *Nat. Commun.* **8**, 14325.

GORDILLO, L. & MUJICA, N. 2014 Measurement of the velocity field in parametrically excited solitary waves. *J. Fluid Mech.* **754**, 590–604.

HENDERSON, D. M. & SEGUR, H. 2013 The role of dissipation in the evolution of ocean swell. *J. Geophys. Res.* **118** (10), 5074–5091.

HOLMEDAL, L. E. & MYRHAUG, D. 2009 Wave-induced steady streaming, mass transport and net sediment transport in rough turbulent ocean bottom boundary layers. *Cont. Shelf Res.* **29**, 911–926.

LESSER, M. B. & BERKLEY, D. A. 1972 Fluid mechanics of the cochlea. Part 1. *J. Fluid Mech.* **51**, 497–512.

LONGUET-HIGGINS, M. S. 1953 Mass transport in water waves. *Proc. R. Soc. Lond.* A **245**, 535–581.

LUCASSEN-REYNDERS, E. H. & LUCASSEN, J. 1970 Properties of capillary waves. *Adv. Colloid Interface Sci.* **2**, 347–395.

MARTÍN, E. & VEGA, J. M. 2006 The effect of surface contamination on the drift instability of standing Faraday waves. *J. Fluid Mech.* **546**, 203–225.

MILES, J. & HENDERSON, D. 1990 Parametrically forced surface waves. *Annu. Rev. Fluid Mech.* **22**, 143–165.

MOISY, F., BOUVARD, J. & HERREMAN, W. 2018 Counter-rotation in an orbitally shaken glass of beer. *Eur. Phys. Lett.* **122**, 34002.

NICOLÁS, J. A. & VEGA, J. M. 2003 Three-dimensional streaming flows driven by oscillatory boundary layers. *Fluid Dyn. Res.* **32** (4), 119–139.

PÉRINET, N., GUTIÉRREZ, P., URRA, H., MUJICA, N. & GORDILLO, L. 2017 Streaming patterns in Faraday waves. *J. Fluid Mech.* **819**, 285–310.

PERLIN, M. & SCHULTZ, W. W. 2000 Capillary effects on surface waves. *Annu. Rev. Fluid Mech.* **32**, 241–274.

PUNZMANN, H., FRANCOIS, N., XIA, H., FALKOVICH, G. & SHATS, M. 2014 Generation and reversal of surface flows by propagating waves. *Nat. Phys.* **10**, 658–663.

RILEY, N. 2001 Steady streaming. *Annu. Rev. Fluid Mech.* **33**, 43–65.

SCHNECK, D. J. & WALBURN, F. J. 1976 Pulsatile blood flow in a channel of small exponential divergencepart. Part II. Steady streaming due to the interaction of viscous effects with convected inertia. *Trans. ASME J. Fluids Engng* **98**, 707–713.

STRICKLAND, S. L., SHEARER, M. & DANIELS, K. E. 2015 Spatiotemporal measurement of surfactant distribution on gravity–capillary waves. *J. Fluid Mech.* **777**, 523–543.

YI, S., DING, H. & SPELT, P. D. M. 2014 Numerical simulations of flows with moving contact lines. *Annu. Rev. Fluid Mech.* **46**, 97–119.

https://doi.org/10.1017/jfm.2020.281 Published online by Cambridge University Press